International Journal of Advanced Materials Research
Vol. 3, No. 1, 2017, pp. 1-8
http://www.aiscience.org/journal/ijamr
ISSN: 2381-6805 (Print); ISSN: 2381-6813 (Online)

Dependence of Upconversion Luminescence and Morphology on the Host Materials

Shigang Hu[1, *], Qingyang Wu[1], Xiaofeng Wu[1], Yunxin Liu[2], Jin Li[1], Shiping Zhan[2], Zhijun Tang[1]

[1]School of Information and Electrical Engineering, Hunan University of Science and Technology, Xiangtan, China
[2]Department of Physics and Electronic Science, Hunan University of Science and Technology, Xiangtan, China

Abstract

Crystal structure, morphology, and optical properties of Tm^{3+}, Er^{3+}, and Yb^{3+} ions doped four types of host materials [$NaLnF_4$, Ln=Y, Lu, Gd, La] have been investigated. X-ray diffraction (XRD), scanning electron microscopy (SEM), and photoluminescence (PL) spectra were used to characterize the samples. For La-based fluoride, the as synthesized microcrystals are assigned to LaF_3 crystal phase. For the other three hosts, hexagonal $NaREF_4$ crystal phase accordingly formed. By changing the dopant's species, strong multicolor upconversion (UC) emissions can be obtained under 980 nm laser diode (LD) excitation. It is found that the up-conversion luminescence is strongly depended on the host material, particle size, doping substances and concentration and internal structure. Importantly, the intensity ratio of green to red emissions and the intensity ratio of blue to red emissions are highly depended on the property of host materials. The UC mechanisms in the four host materials are also discussed.

Keywords

Rare Earth, Upconversion Luminescence, Microcrystals, Hydrothermal Method

Received: February 22, 2017 / Accepted: April 7, 2017 / Published online: June 14, 2017

1. Introduction

With abundant f-orbital configurations, lanthanide (Ln) ions can exhibit sharp fluorescent emissions via intra-4f or 4f−5d transitions and thus are widely used as emitting species in many phosphors [1-2]. Compared with lanthanide chelates, quantum dots (QDs), and organic dye molecules, Ln^{3+}-doped inorganic materials hold all the advantages of a large Stokes shift, a sharp emission spectrum, a long lifetime, high chemical/photochemical stability, low toxicity, and reduced photobleaching [3-6]. Ln^{3+}-doped inorganic materials are widely applied in the fields of lasers, displays, sensors, solar cells, electroluminescent devices, and biomedical research [7-9].

Much attention has been paid to the up-conversion (UC) process, which is a successful method to generate visible light from long-wavelength excitation of near-infrared (NIR) light [10-12]. The use of lower energy excitation is associated with several significant advantages, such as negligible photobleaching damage to living organisms, low autofluorescence background, and high light excitation penetration depth in biological tissues [13].

In order to obtain efficient UCL, selection of host matrixis is very important for achieving efficient UC luminescence. Among all of the investigated UC host materials such as oxides, fluorides, and vanadates, Ln doped fluorides ($NaLnF_4$) are considered as the most efficient one for UC emission due to their low phonon energy, which decreases

* Corresponding author
E-mail address: hsg99528@126.com (Shigang Hu)

the non-radiative relaxation probability [14-15]. Er^{3+} and Tm^{3+} ions with ladder-like energy levels are the most common activators to generate UCL under 980 nm NIR excitation. In addition, because Yb^{3+} ion possesses a larger absorption cross section to 980 nm pump photons than that of other Ln^{3+} ions, it is usually selected as a particularly and efficient sensitizer for enhancing the luminescent efficiency of emitters Er^{3+} and Tm^{3+}. Furthermore, the energy gap between ground state and the only excited state of Yb^{3+} matches well with the energy differences of Er^{3+}/Tm^{3+} which allows for efficient (quasi) resonant energy transfer from Yb^{3+} to Er^{3+}/Tm^{3+} ions and further enhances the UCL.

In the present work, crystal structure, morphology and optical properties of various host crystals doped with optically active ions Er^{3+}/Tm^{3+} have been investigated.

2. Experimental

All rare earth oxides used were of 99.99% purity. Rare earth nitrate $RE(cl)_3$ (RE Lu, La, Gd,Y, Yb, Er and Tm) solutions were prepared by dissolving the corresponding rare earth oxides in hydrochloric acid at a high temperature. All other chemicals were analytical grade and used without further purification.

2.1. Synthesis of Ln^{3+}-doped Fluorides Microcrystals

Ln^{3+}-doped fluorides microcrystals were synthesized by a hydrothermal method using trisodium citrate as a stabilizing surfactant. 0.294g of trisodium citrate and 10 mL of de-ionized water were mixed together under agitation to form a homogeneous solution. Subsequently, 1 mmol $RECl_3$ (RE Lu, Y, Gd, La, Yb, Er or Tm with designed molar ratios) and 16 mL of 8 mmol NaF solutions were added under constant vigorous stirring for 10–20 min. The resulting solution was transferred to a 50 mL autoclave, sealed, and hydrothermally treated at a designed temperature of 180°C for 10h. After reaction completion, the system was naturally cooled to room temperature. The resulting samples were washed several times with ethanol and de-ionized water to remove residual solvents, and then dried at 60℃ for 24h. The rare earth element of host material can be one of the four elements Y, Lu, Gd and La. The doped styles of rare earth elements in fluoride were Yb^{3+}(18%)/Er^{3+}(2%) co-doped, Yb^{3+}(20%)/Tm^{3+}(0.5%) co-doped and Yb^{3+}(5%)/Er^{3+}(0.5%)/Tm^{3+}(0.5%) tri-doped respectively.

2.2. Characterization

The phase identification was performed by X-ray diffraction (XRD) (D8 Advance), using nickel-filtered Cu-Ka radiation (λ=1.5406 Å). The step scan covered the angular range from 10° to 70°. The morphologies of products were observed using a scanning electron microscope(SEM) (JSM-6380LV). Upconversion emission spectra of the samples were recorded with a fluorescence spectrophotometer(Hitachi F-2700). A 980 nm laser diode with the maximum power of 0.1w was employed as the upconversion pump source.

3. Results and Discussion

3.1. Yb^{3+}/Er^{3+} Co-doped $NaLnF_4$ (Ln=Y, Lu, Gd, La)

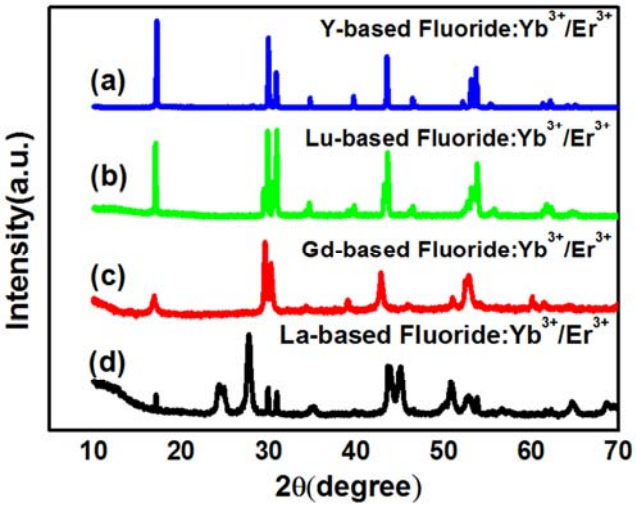

Figure 1. XRD patterns of four fluorides with the same Yb^{3+}(18%)/Er^{3+} (2%) co-doping: (a) Y-based fluoride, (b) Lu-based fluoride, (c) Gd-based fluoride, (d) La-based fluoride.

The crystal structures and the phase purity of the as-prepared products were determined by XRD spectra. Typical XRD patterns of four host materials are presented in Figure 1. The diffraction peaks in curve (a)-(c) can be indexed to the pure hexagonal $NaYF_4$ (JCPDS 16-0334), $NaLuF_4$ (JCPDS 27-0276) and $NaGdF_4$ (JCPDS 27-0699). No other impurity peaks were detected, demonstrating the successful incorporation of all the Yb^{3+} and Er^{3+} ions into the three host matrixes and formed solid solution structure. Noticeable for La-based host as shown in Figure 1 (d), the as synthesized microcrystals consist of two phases, i.e., the hexagonal LaF_3 (JCPDS 32-0483) and the hexagonal phase $NaYbF_4$ (27-1427). It can be seen from Figure 1 that the diffraction peaks of Gd-based fluoride: Yb^{3+}/Er^{3+} and La-based fluoride: Yb^{3+}/Er^{3+} are wider than the other two, indicating that they have smaller particle size, which is further verified by SEM measurement.

To further reveal the phase and size control, the as-prepared microcrystals were characterized by SEM, which are presented in Figure 2. It can be seen that the host compositions have significant influence on the corresponding morphologies of the products. Figure 2 (a) illustrates the

representative SEM image of $NaLuF_4$:Yb^{3+}/Er^{3+} microcrystals. The morphology of $NaLuF_4$: Yb^{3+}/Er^{3+} shows hollow irregular hexagonal prism. It can be clearly seen that these microrods open at both ends. The detailed structure of $NaLuF_4$: Yb^{3+}/Er^{3+} microcrystals is shown in Figure 2 (b) that hexagonal mircoplates with both smooth side facets and top–bottom surfaces and relatively uniform size are formed. We note that the hydrothermal synthesized β-$NaGdF_4$ in these conditions show enhanced (110) XRD peak in comparison with the standard card of β-$NaGdF_4$. This result implies the presence of preferred growth direction dependent on morphology of the product. The synthesized submicron β-$NaGdF_4$:Yb^{3+}/Er^{3+} shows hexagonal prism. It is interesting to find that $NaLaF_4$:Yb^{3+}/Er^{3+}exhibits irregular morphologies. As shown in Figure 2 (d), nanoparticles and microtubes are observed clearly. From SEM images in Figure 2, it is clear that the morphology of $NaLnF_4$ is highly depended on the host Ln^{3+} ion if the reaction time and temperature and the doping are fixed as the same ones.

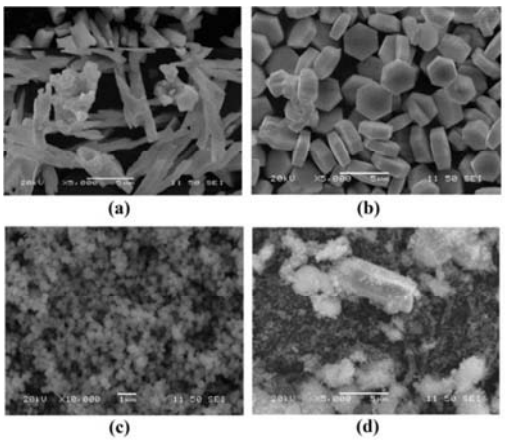

Figure 2. SEM images of four fluorides with the same Yb^{3+}(18%)/Er^{3+}(2%) co-doping: (a) Y-based fluoride, (b) Lu-based fluoride, (c) Gd-based fluoride, (d) La-based fluoride.

Subsequently, the upconversion fluorescence spectra of the sample with various compositions were recorded under excitation of a 980 nm LD of as low as 20mW with a spectrophotometer (F2700). All the samples can emit dazzlingly bright light. As shown in Figure 3, the 18% Yb^{3+}, 2% Er^{3+} co-doped four fluorides show three dominant emission peaks centered at 528, 543, and 660nm, which are assigned to the $^2H_{11/2}\rightarrow{}^4I_{15/2}$, $^4S_{3/2}\rightarrow{}^4I_{15/2}$ and $^4F_{9/2}\rightarrow{}^4I_{15/2}$ transitions of Er^{3+} ion, respectively. The luminous intensities of Gd-based fluoride: Yb^{3+}/Er^{3+} and La-based fluoride:Yb^{3+}/Er^{3+} are weaker than the other two, because they have smaller particle size. In addition, the weak blue ($^2H_{9/2}\rightarrow{}^4I_{15/2}$:408 nm) emission band has also been observed in Yb^{3+}/Er^{3+} co-doped fluorides microcrystals. The observation of 408 nm emission provides a direct evidence for the high UC efficiency of the Yb^{3+}/Er^{3+} co-doped fluorides microcrystals. It should be noted the intensity of green emission peak is weaker than that of red emission peak in La-based fluoride:Yb^{3+}/Er^{3+} as shown in Figure 3 (d). It is quite clear from Figure 4 that the Intensity Ratio of the Green to Red (IRGR) emission varies with the change of host matrix. The IRGR of La-based fluoride:Yb^{3+}/Er^{3+} is lower than 1, while those of the others are larger than 1. The Gd-based fluoride: Yb^{3+}/Er^{3+} has the IRGR value.

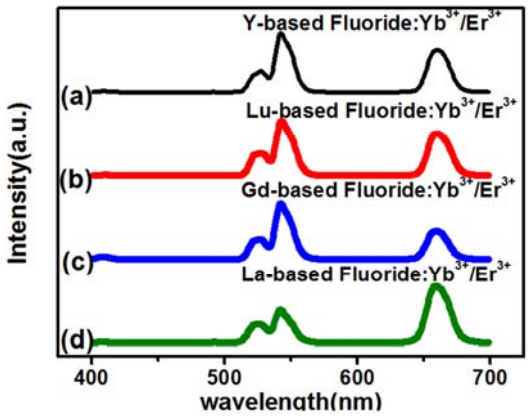

Figure 3. Upconversion luminescence spectra of four fluorides with the same Yb^{3+}(18%)/Er^{3+} (2%) co-doping: (a) Y-based fluoride, (b) Lu-based fluoride, (c) Gd-based fluoride, (d) La-based fluoride.

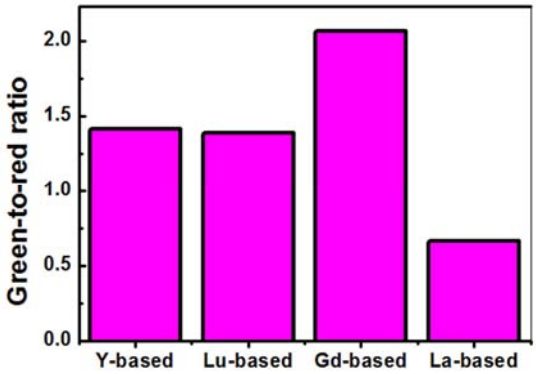

Figure 4. Green-to-red intensity ratios of Yb^{3+}/Er^{3+} co-doped fluorides microcrystals.

In Yb^{3+} and Er^{3+} co-doped $NaLnF_4$ microcrystals, the proposed UC mechanisms can be described as follows (Figure 5): First, an excited Yb^{3+} ion in the $^2F_{5/2}$ state transfers its energy to an Er^{3+} ion to populate the $^4I_{11/2}$ level. Second, The Er^{3+} ion can decay nonradiatively to $^4I_{13/2}$ and then absorbs a second pump photon to an upper level $^4F_{9/2}$ level, which can also lead to the dominant red emission $^4F_{9/2}\rightarrow{}^4I_{15/2}$. Alternatively, after populating the $^4I_{11/2}$ level, energy transfer from an Yb^{3+} ion can then populate the $^4F_{7/2}$ level of the Er^{3+} ion. The Er^{3+} ion can then decay nonradiatively to the $^2H_{11/2}$ and $^4S_{3/2}$ levels lead to the dominant $^2H_{11/2}/^4I_{15/2}$ and $^4S_{3/2}/^4I_{15/2}$ transitions, and nonradiative decay from $^2H_{11/2}/^4S_{3/2}$ may directly populate $^4F_{9/2}$ state and result in another dominant red $^4F_{9/2}\rightarrow{}^4I_{15/2}$ emission. In addition, the Er^{3+} ion

in the $^4F_{9/2}$ level can be promoted to the level $^2H_{9/2}$ and resulting in weak violet emission.

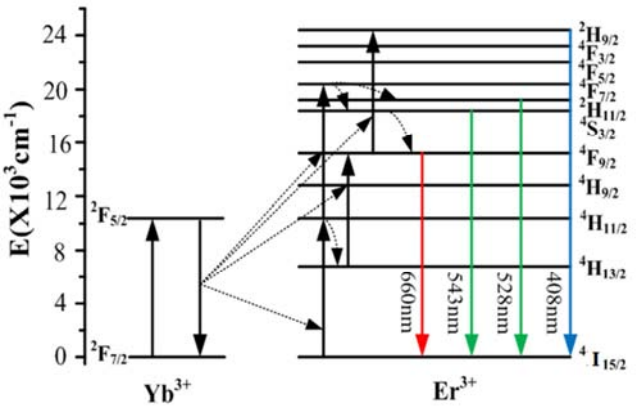

Figure 5. Schematic energy-level diagram of Yb^{3+} and Er^{3+}, and the proposed mechanism of upconversion emissions.

3.2. Yb^{3+}/Tm^{3+} Co-doped $NaLnF_4$ (Ln=Y, Lu, Gd, La)

The phase compositions of the as-prepared Yb^{3+} and Tm^{3+} co-doped rare earth fluorides were detected by the powder XRD pattern as shown in Figure 6. The XRD pattern curves in Figure 6 (a)-(c) are characteristic of hexagonal phase $NaReF_4$. The observed results are similar to that of Figure 1. However, some of the relative intensities of the diffraction peaks are different. There are also two phases in Yb^{3+} and Tm^{3+} co-doped La-based fluoride. Despite the doping component varies from Yb^{3+}/Er^{3+} to Yb^{3+}/Tm^{3+}, the morphologies of the four fluorides microcrystals remain substantially unchanged as shown in Figure 7. These results indicate that the substitution of small amount of Er^{3+} ion by Tm^{3+} ion has no obvious influence on the crystal structure and morphology.

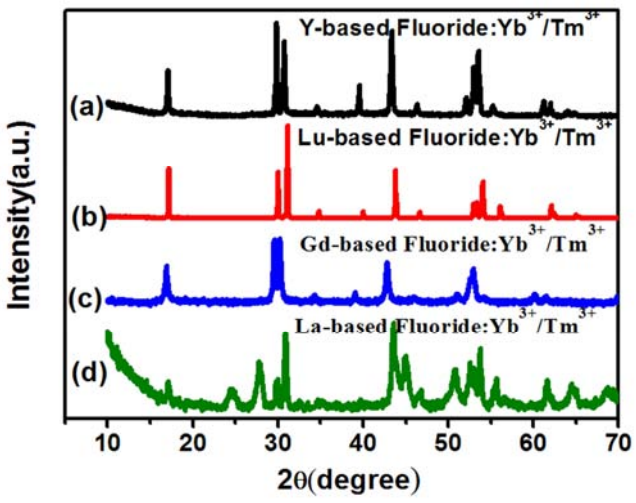

Figure 6. XRD patterns of four fluorides with the same Yb^{3+}(20%)/Tm^{3+} (0.5%) co-doping: (a) Y-based fluoride, (b) Lu-based fluoride, (c) Gd-based fluoride, (d) La-based fluoride.

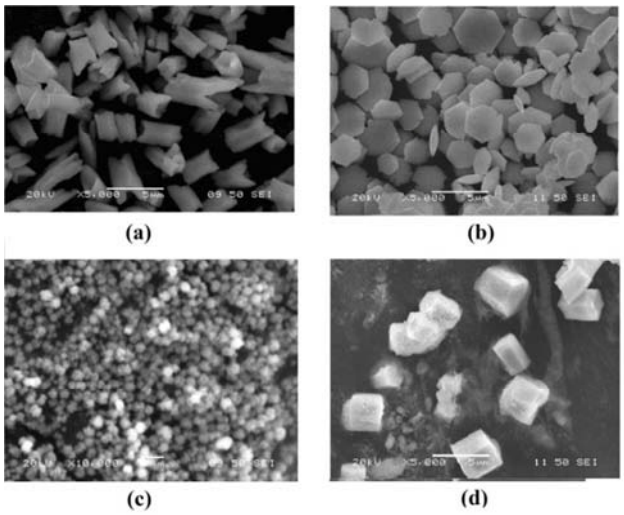

Figure 7. SEM images of four fluorides with the same Yb^{3+}(20%)/Tm^{3+} (0.5%) co-doping: (a) Y-based fluoride, (b) Lu-based fluoride, (c) Gd-based fluoride, (d) La-based fluoride.

Figure 8 presents the UC emission spectrum of Yb^{3+} and Tm^{3+} co-doped rare earth fluorides under 980 nm excitation. The blue and red emissions centered at 450, 474, 646 and 697 nm are observed, which are attributed to the $^1D_2 \rightarrow {}^3F_4$, $^1G_4 \rightarrow {}^3H_6$, $^1G_4 \rightarrow {}^3F_4$ and $^3F_3 \rightarrow {}^3H_6$ transitions of Tm^{3+}, respectively. The blue-to-red intensity ratios (BRR) of Yb^{3+}/Tm^{3+} co-doped fluorides microcrystals are shown in Figure 9. The IRGR of La-based fluoride: Yb^{3+}/Tm^{3+} is equal to 2, while those of the others is greater than 10. The IRGR of Gd-based fluoride: Yb^{3+}/Tm^{3+} is the largest one.

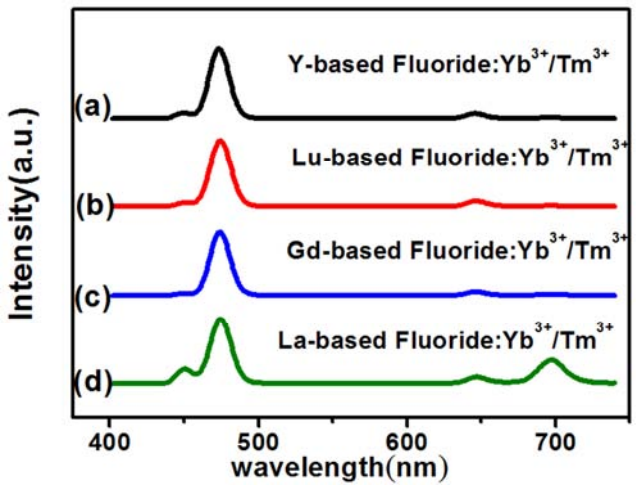

Figure 8. Upconversion luminescence spectra of four fluorides with the same Yb^{3+}(20%)/Tm^{3+} (0.5%) co-doping: (a) Y-based fluoride, (b) Lu-based fluoride, (c) Gd-based fluoride, (d) La-based fluoride.

According to the simplified energy level diagram shown in Figure 10, the possible upconversion mechanisms have been discussed in detail. In the first step of excitation, a pump photon at 980 nm provokes the excitation of the Yb^{3+} sensitizer from the $^2F_{7/2}$ ground state to the $^2F_{5/2}$ excited state. The excited Yb^{3+} ion transfers its energy to a neighbor Tm^{3+}

ion for the $^3H_6 \rightarrow {}^3H_5$ transition of Tm^{3+} ion. The Tm^{3+} ion populated in the $^3H_5$ level will decay nonradiatively to $^3F_4$ level by the multiphonon relaxation, and then absorbs a second pump photon to an upper level $^3F_2$ level. The Tm^{3+} ion populated in the $^3F_2$ level will decay nonradiatively to $^3F_3$, $^3H_4$, and $^3F_4$. The transitions of $^3F_3$ to $^3H_6$ level emit the red emissions at 697nm. The Tm^{3+} then absorbs a third pump photon to an upper level $^1G_4$ level, which can yield red and blue emissions upon radiative relaxation back to $^3F_4$ and $^3H_6$ levels, respectively. There is another energy transfer process from Yb^{3+} to Tm^{3+} ions which may take place to populate the Tm^{3+} from $^1G_4$ to $^1D_2$. However, this energy transfer way is usually less efficient due to the relative large energy mismatch. Therefore, the cross relaxation (CR) process of $^3F_2+{}^3H_4 \rightarrow {}^3H_6+{}^1D_2$ between Tm^{3+} ions may alternatively play an important role in populating $^1D_2$ level, which subsequently resulting in the blue emission band centered at 450 nm. However, because of the poor CR process of Tm^{3+} ions, the intense of the blue emission centered at 450nm is much weaker compared with the blue emission band centered at 474 nm.

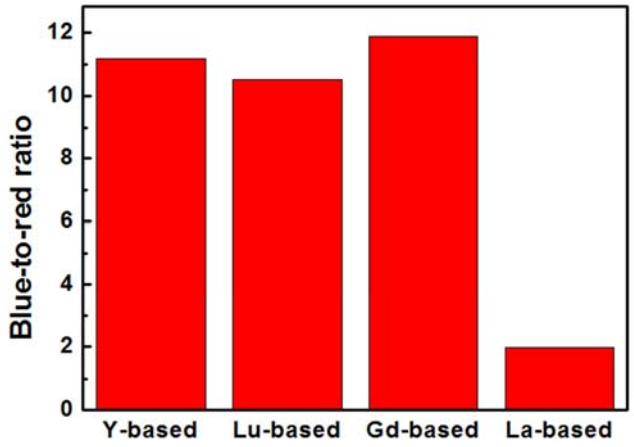

Figure 9. Blue-to-red intensity ratios of Yb^{3+}/Tm^{3+}co-doped fluorides microcrystals.

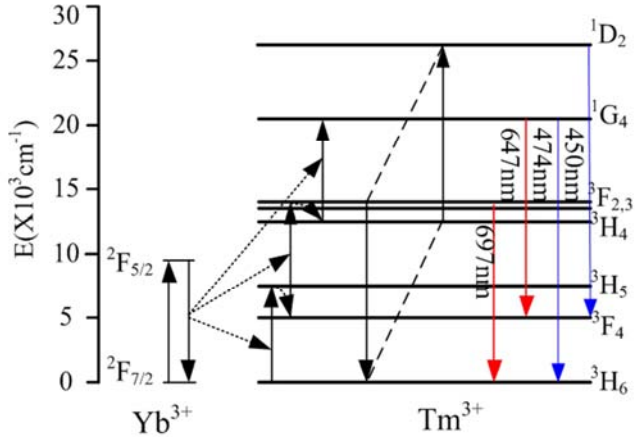

Figure 10. Schematic energy-level diagram of Yb^{3+} and Tm^{3+}, and the proposed mechanism of upconversion emissions.

3.3. $Yb^{3+}/Er^{3+}/Tm^{3+}$ Tri-doped $NaLnF_4$ (Ln=Y, Lu, Gd, La)

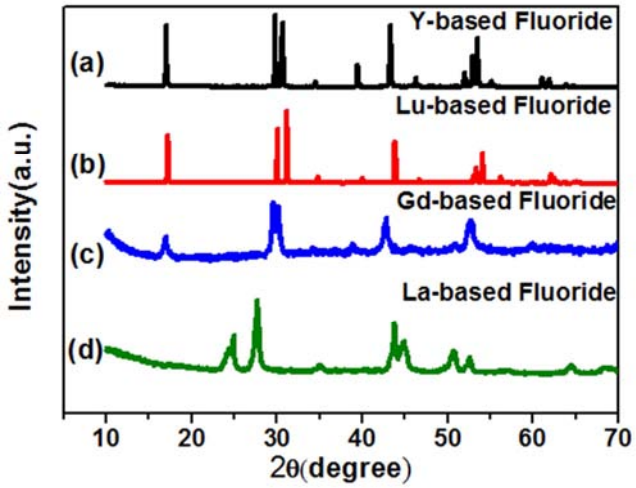

Figure 11. XRD patterns of four fluorides with the same Yb^{3+}(5%)/Er^{3+} (0.5%) /Tm^{3+} (0.5%) tri-doping: (a) Y-based fluoride, (b) Lu-based fluoride, (c) Gd-based fluoride, (d) La-based fluoride.

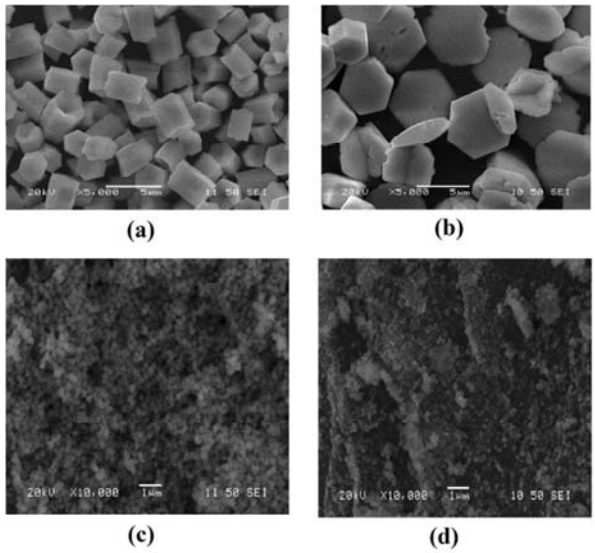

Figure 12. SEM images of four fluorides with the same Yb^{3+}(5%)/Er^{3+} (0.5%) /Tm^{3+} (0.5%) tri-doping: (a) Y-based fluoride, (b) Lu-based fluoride, (c) Gd-based fluoride, (d) La-based fluoride.

The XRD patterns of the $Yb^{3+}/Er^{3+}/Tm^{3+}$ tri-doped materials are shown in Figure 11. The positions and relative intensity of diffraction peaks in Figure 11 (a)-(c) can be indexed well to those standard cards of the hexagonal $NaReF_4$ (RE= Y, Lu, Gd) accordingly. No second phase is detected in all XRD patterns, which indicates that the Ln^{3+} ions have been effectively doped into the host lattices. But for the XRD pattern of La-based fluoride as shown in Figure 11 (d), it is basically consistent with the XRD standard card No. 32-0483 of hexagonal LaF_3. Figure 12 shows the SEM images of the tri-doped materials. It should be noted that only nanoparticles can be observed in the tri-doped La-based fluoride as shown

in Figure 12 (d), which is different from that in the co-doped La-based fluoride. It may be due to the effect of Yb^{3+} ion concentration on the morphology of La-based fluoride, when the concentration is low, the single phase fluoride crystal can be formed. The morphologies of the other three fluorides microcrystals remain substantially unchanged.

Figure 13 shows the upconversion luminescence spectra of the tri-doped materials, two distinctive emission bands come from the green emissions (507–572 nm, centered at 524 and 543) and the red emission (630–696 nm, centered at 659 nm). In addition, weak violet emission centered at 407nm and intense blue emission centered at 474 nm have also been observed in Yb^{3+}/Er^{3+} /Tm^{3+} tri-doped fluorides microcrystals. The relative intensity of red emission is increased significantly, which is due to a fact that both Er^{3+} and Tm^{3+} can emit red emission. However, the blue emission intensity is weakened, which indicated that the ET from Er^{3+} to Tm^{3+} was efficient and much of the mission intensities of Tm^{3+} ions transferred to Er^{3+} ions. In the tri-doped system, on the one hand, there exists the upconversion luminescence of Er^{3+} and Tm^{3+}; on the other hand, the energy transfer between Er^{3+} and Tm^{3+} make some part of conversion emissions can be weakened. The IRGR of tri-doped fluorides microcrystals are shown in Figure 14. The IRGR of Lu-based and La-based fluorides are larger than 1, while those of the other two are smaller than 1. The La-based fluoride: $Yb^{3+}/Tm^{3+}/Er^{3+}$ have the largest IRGR value.

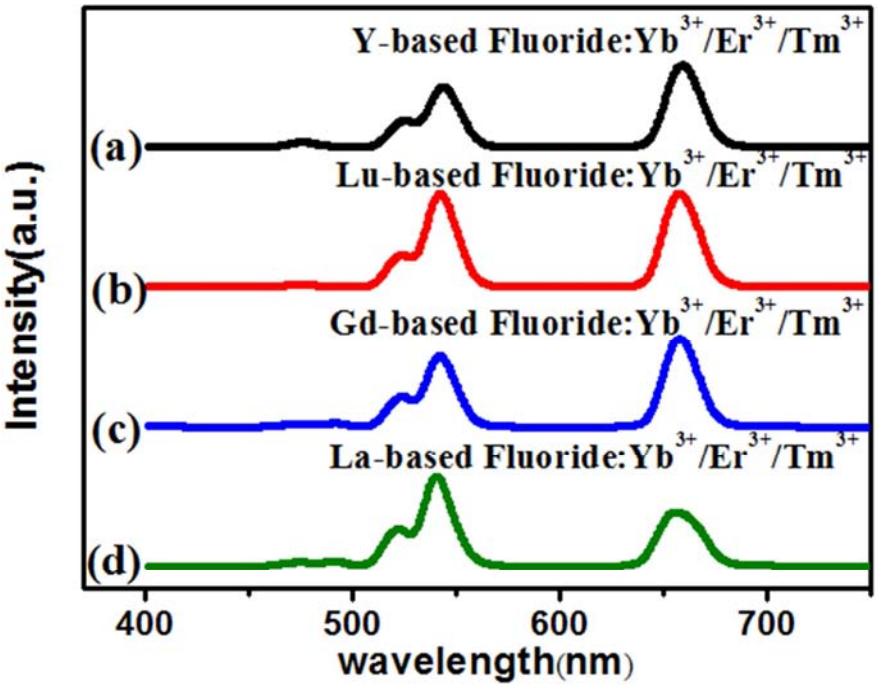

Figure 13. Upconversion luminescence spectra of four fluorides with the same Yb^{3+}(5%)/Er^{3+} (0.5%) /Tm^{3+} (0.5%) tri-doping: (a) Y-based fluoride, (b) Lu-based fluoride, (c) Gd-based fluoride, (d) La-based fluoride.

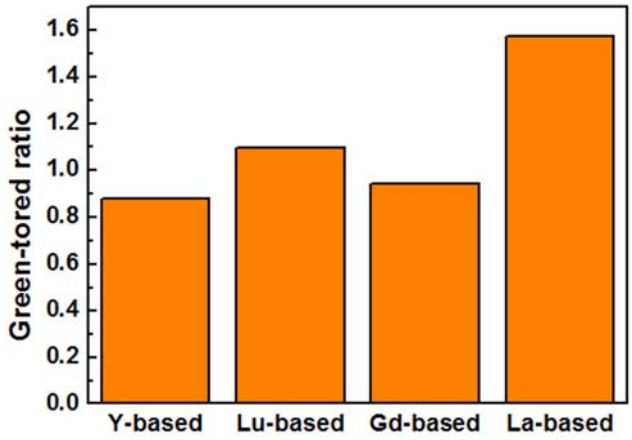

Figure 14. Green-to-red intensity ratios of $Yb^{3+}/Er^{3+}/Tm^{3+}$ co-doped fluorides microcrystals.

The schematic energy levels diagram of Er^{3+}, Tm^{3+}, Yb^{3+} ions in the fluorides microcrystals and upconversion processes under 980 nm excitation is shown in Figure 15. After absorption of photons by Yb^{3+}, energy transfer (ET) takes place between Yb^{3+}, $Er^{3+}$and Tm^{3+}. Under 980nm excitation, the Yb^{3+} ions are excited from the $^2F_{7/2}$ level to the $^2F_{5/2}$ level, then transfer their energies to the nearby $Er^{3+}$and Tm^{3+}ions, then three successive ET fromYb^{3+} toTm^{3+} populate the $^3H_5$, $^3F_2$, and $^1G_4$ levels of Tm^{3+}. The Tm^{3+} ions on $^3H_5$ and $^3F_2$ states will nonradiative transmit to $^3F_4$ and $^3H_4$ states respectively. Similarly, three successive ET processes make Er^{3+} populate the $^4I_{11/2}$, $^4F_{9/2}$, and $^2H_{9/2}$ levels. The Er^{3+} ions on $^4F_{11/2}$ and $^4F_{7/2}$ states will nonradiative transmit to $^4F_{13/2}$, and $^2H_{11/2}$/$^4S_{3/2}$ states, Finally, the blue emission centered at 474nm is generated by transition of Tm^{3+} ions $^1G_4 \rightarrow {}^3H_6$; The

green emission between 507 and 572 nm is due to transitions from Er^{3+} ions on $^2H_{11/2}$ and $^4S_{3/2}$ excited states to the $^4I_{15/2}$ ground state; the red emission between 630 and 696 nm arises from the $^4F_{9/2}\rightarrow{}^4I_{15/2}$ transition of Er^{3+} and $^3F_{2,3}\rightarrow{}^3H_6$ of Tm^{3+}, the blue emission centered at 407 nm is generated by transition of Er^{3+} ions $^2G_{9/2}\rightarrow{}^4I_{15/2}$ transition.

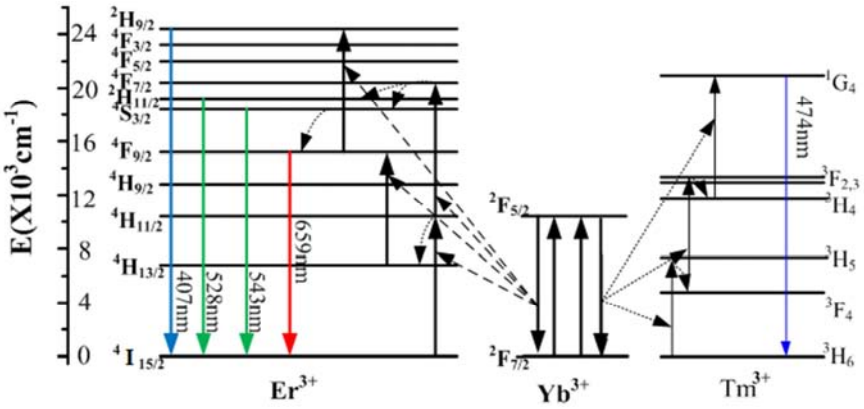

Figure 15. Schematic energy levels diagram of Er^{3+}, Tm^{3+}, Yb^{3+} ions in the fluorides microcrystals and upconversion processes under 980 nm excitation.

4. Conclusions

In summary, we have demonstrated a facile hydrothermal method for the synthesis of Ln^{3+}-doped fluorides with different phases and morphologies by fixing the reaction temperature and time and the doping. The multiform microstructures can be achieved by conveniently adjusting two kinds of experimental parameters such as host material(Y, Lu, Gd and La) and dopant's species(Yb^{3+}/Er^{3+} co-doped, Yb^{3+}/Tm^{3+} co-doped, $Yb^{3+}/Er^{3+}/Tm^{3+}$ tri-doped). The XRD and SEM analysis reveal that Gd-based and La-based host can easily generate small particle, while the other two hosts prefer to form crystals with larger particle size; for La-based fluoride, the as synthesized microcrystals are assigned to LaF_3 crystal phase; for other rare earth ions doped fluoride, stable hexagonal-phased β-$NaREF_4$ can be formed. There are two phases existing in Yb^{3+} /Tm^{3+} and Yb^{3+}/Er^{3+} co-doped La-based fluoride, it is attributed to the large concentration of Yb^{3+} ions. Intensive multicolor up-conversion luminescence under the excitation of 980 nm has been successfully realized by doping different lanthanide ions into the host lattices. In Yb^{3+}/Er^{3+} co-doped rare earth fluorides, the upconverting green band centered at 543/528 nm and red band centered at 660 nm were simultaneously observed under the excitation of a 980 infrared diode laser. Especially, IRGR of the upconversion emission of the Yb^{3+}/Er^{3+} co-doped $NaREF_4$ can be tuned by changing the host composition. In Yb^{3+}/Tm^{3+} co-doped $NaREF_4$, the upconverting blue band centered at 450/474 nm and red band centered at 647/690 nm were simultaneously observed. IRGR of the upconversion emission of the Yb^{3+}/Tm^{3+} co-doped can be tuned with the change of host material. Similarly, IRGR changed with the host composition in the $Yb^{3+}/Er^{3+}/Tm^{3+}$ tri-doped rare earth fluorides.

Acknowledgement

This research was financially supported by the National Natural Science Foundation of China (Grant Nos 61674056, 61675067, 61575062 and 61474042); supported by the Scientific Research Fund of Hunan Provincial Education Department (Grant Nos 16A072 and 16C0627).

References

[1] C. Li, J. Lin, "Rare earth fluoride nano-/microcrystals: synthesis, surface modification and application". Journal of Materials Chemistry, vol. 20, pp.6831-6847, 2010.

[2] J. C. G. Bünzli, "Lanthanide luminescence for biomedical analyses and imaging", Chemical reviews, vol. 110, pp. 2729-2755, 2010.

[3] C. Bouzigues, T. Gacoin, A. Alexandrou, "Biological applications of rare-earth based nanoparticles", ACS nano, vol. 5, pp.8488-8505, 2011.

[4] Y. Liu, S. Zhou, D. Tu, Z. Chen, M. Huang, H. Zhu, X. Chen, "Amine-functionalized lanthanide-doped zirconia nanoparticles: optical spectroscopy, time-resolved fluorescence resonance energy transfer biodetection, and targeted imaging", Journal of the American Chemical Society, vol. 134, pp.15083-15090, 2012.

[5] J. Yao, M. Yang, Y. Duan, "Chemistry, Biology, and Medicine of Fluorescent Nanomaterials and Related Systems: New Insights into Biosensing, Bioimaging, Genomics, Diagnostics, and Therapy", Chemical reviews, vol. 114, pp.6130-6178, 2014.

[6] S. Gai, C. Li, P. Yang, J. Lin, "Recent progress in rare earth micro/nanocrystals: soft chemical synthesis, luminescent properties, and biomedical applications", Chemical reviews, vol. 114, pp.2343-2389, 2013.

[7] K. Binnemans, "Lanthanide-based luminescent hybrid materials", Chemical reviews, vol. 109, pp.4283-4374, 2009.

[8] Bünzli, J. C. G., Eliseeva, S. V., "Lanthanide NIR luminescence for telecommunications, bioanalyses and solar energy conversion", Journal of Rare Earths, vol.28, pp.824-842, 2010.

[9] K. Panthi, R. M. Adhikari, T. H. Kinstle, "Visible and near IR emitting organic nanoparticles of aromatic fumaronitrile core-based donor–acceptor compounds", Journal of Photochemistry and Photobiology A: Chemistry, vol. 215, pp.179-184, 2010.

[10] J. Zhou, G. Chen, E. Wu, G. Bi, B. Wu, Y. Teng, J. Qiu, "Ultrasensitive polarized up-conversion of Tm^{3+}–Yb^{3+} doped β-$NaYF_4$ single nanorod", Nano letters, vol. 13, pp.2241-2246, 2013.

[11] F. He, P. Yang, D. Wang, N. Niu, S. Gai, X. Li, "Self-Assembled β-$NaGdF_4$ Microcrystals: Hydrothermal Synthesis, Morphology Evolution, and Luminescence Properties", Inorganic chemistry, vol. 50, pp.4116-4124, 2011.

[12] X. Li, S. Gai, C. Li, D. Wang, N. Niu, F. He, P. Yang, "Monodisperse lanthanide fluoride nanocrystals: synthesis and luminescent properties", Inorganic chemistry, vol. 51, pp.3963-3971, (2012).

[13] Chen, G., Qiu, H., Prasad, P. N., Chen, X., "Upconversion nanoparticles: design, nanochemistry, and applications in theranostics", Chemical reviews, vol.114, pp.5161-5214, 2014.

[14] Zhao, G., Tong, L., Cao, P., Nitz, M., Winnik, M. A. "Functional PEG–PAMAM-Tetraphosphonate Capped $NaLnF_4$ Nanoparticles and their Colloidal Stability in Phosphate Buffer", Langmuir, vol. 30, pp.6980-6989, 2014.

[15] E. He, H. Zheng, W. Gao, Y. Tu, Y. Lu, G. Li, "Investigation of upconversion and downconversion fluorescence emissions from β-$NaLn1F_4$: Yb^{3+}, $Ln2^{3+}$(Ln1= Y, Lu; Ln2= Er, Ho, Tm, Eu) hexagonal disk system", Materials Research Bulletin, vol. 48, pp. 3505-3512, 2013.